Int j simul model 24 (2025) 3, 509-520
Original scientific paper

CFD-EXPERIMENTAL STUDY ON THERMOFLOW IN RICE HULLER CHAMBER

Feng, Y. T.*; Peng, J. S.*,#; Tang, Z. S.*; Yang, X.* & Huang, W.**
* Geely University of China, Chengdu 641423, China
** School of Mechanical Engineering, Xihua University, Chengdu 610039, China
E-Mail: fengyetao917@163.com, pengjianshe2005@163.com (# Corresponding author)

Abstract
To optimize the design of the hulling chamber structure in rubber-roller paddy hullers and reduce broken rice rate during hulling processing, this study takes a rubber-roller paddy huller as the research object. First, experiments were designed and conducted to analyse the temperature and airflow distribution within the hulling chamber. Second, numerical simulations of the temperature field and flow field inside the hulling chamber were performed based on fluid dynamics principles. Subsequently, comparative analysis between numerical simulation results and experimental data was conducted to validate the turbulence model, mesh generation, and boundary condition settings. This verification ensures the accuracy and rationality of the numerical simulation methodology for temperature and flow fields. The comparative results demonstrate temperature errors within 13.5 % and velocity vector errors within 15 %, confirming the feasibility and rationality of the proposed numerical simulation approach for temperature and flow field analysis.
(Received in April 2025, accepted in May 2025. This paper was with the authors 2 weeks for 2 revisions.)

Key Words: Numerical Simulation, Temperature Field, Flow Field, Experiment, Rubber-Roller Paddy Huller

1. INTRODUCTION

Rice processing constitutes the pivotal stage in post-harvest grain handling, where the hulling operation critically determines brown rice yield, energy consumption, and subsequent milling efficiency [1]. As the dominant hulling equipment, rubber-roller paddy hullers utilize shear forces generated by differential roller speeds to achieve husk separation. The multiphysics-coupled environment within the hulling chamber fundamentally governs equipment performance.

The hulling chamber, serving as the core functional zone, exhibits pronounced spatial heterogeneity in its thermal and flow fields. Transient thermal loads from roller friction generate peak temperatures of 50–60 °C, inducing rice protein denaturation and increased endosperm brittleness [2]. Concurrently, the airflow structure directly impacts husk-bran separation efficiency: optimized air currents not only facilitate material separation but also reduce chamber temperature, thereby lowering broken rice rates [3-4]. Suboptimal vortex distribution elevates husk residue retention, while localized overheating on roller surfaces accelerates rubber aging, shortening service life by 30–40 %. Current equipment designs predominantly rely on empirical formulas, lacking systematic understanding of temperature-flow field coupling mechanisms, thus leaving substantial room for optimization.

This study systematically investigates the multiphysics coupling in rubber-roller hullers, with key innovations including:

(1) Development of a multi-parameter synchronous testing platform integrating UTi260B infrared thermography and DT-8880 thermal anemometry, enabling in situ dynamic acquisition of 3D temperature and flow fields;

(2) Establishment of a parametric finite element model employing Realizable k-ε turbulence model coupled with energy equations, enhanced by hexahedral mesh local refinement techniques for improved contact heat transfer simulation accuracy;

(3) Creation of a dual-dimensional error verification system achieving cross-validation between experimental and simulated values through spatial mapping of 6 temperature measurement points and 5 velocity measurement points (temperature error ≤13.5 %, velocity error ≤15 %). This research transcends traditional empirical design limitations, providing theoretical foundations for huller structural optimization.

Through combined experimental and computational fluid dynamics (CFD) approaches, this work elucidates the frictional heat conduction mechanisms and vortex evolution characteristics by analysing 3D temperature/flow field distributions. The findings support the development of multi-objective optimization models for hulling chambers, driving advancements in high-efficiency, low-damage rice processing equipment. The proposed test-simulation bidirectional validation methodology establishes a novel framework for multiphysics analysis of complex agricultural equipment cavities, with broad applicability in grain processing and drying machinery.

2. STATE OF THE ART

In recent years, experimental and simulation methodologies have been extensively adopted. Sfeir employed hot-wire anemometry to measure the mean velocity and temperature distributions of rectangular jets with varying aspect ratios and nozzle geometries [5]. Hao et al. developed a purpose-specific integrated model to identify three types of strip surface quality defects, establishing a methodological foundation for related research [6]. Kevorkijan et al. employed numerical simulations to compare diverse driving pressure methodologies, quantitatively evaluating cavitation initiation efficacy during acoustic pressure transmission from the source to the surface [7].

Concurrently, research on thermal and flow fields has witnessed significant advancements. The progressive optimization of fuel cell cooling flow fields by Rahimi-Esbo et al. demonstrated that the Temperature Uniformity Index (*IUT*) serves as an effective thermal management evaluation metric [8]. Furthermore, Pastohr et al. validated the consistency between simplified algorithms and CFD results through inverse wind farm modelling, with their parametric modelling approach laying the groundwork for rapid development of predictive models [9].

Flow field characteristics critically govern heat-mass transfer efficiency and particle trajectories. Li et al. developed a novel three-dimensional wavy-serpentine flow field (WSFF) through integrated simulation and experimental approaches, systematically analysing its hydrodynamic performance [10]. Zhou and Rempfer conducted numerical investigations on nonlinear two-dimensional unsteady flow fields of Savonius-type and Bach-type rotors, establishing a predictive simulation framework for their aerodynamic characteristics [11]. The numerical study by Xiang and Lee on cyclone separator tangential velocity fields revealed that geometric configuration modifications induce significant flow field distortions [12]. Salaheldin et al. accurately resolved three-dimensional flow structures around bridge piers using Reynolds Stress Models (RSM), with their turbulence modelling expertise providing essential parameter calibration benchmarks for high-speed shear flow simulations [13]. Kumar and Nigan identified Dean vortex-enhanced heat transfer phenomena in reverse helical pipe flows, whose chaotic mixing mechanisms established a theoretical foundation for analysing secondary flows induced by roller rotation [14]. Furthermore, Lim and Lee enhanced kitchen exhaust system efficiency through separation plate configurations, demonstrating that localized flow-guiding structures can optimize temperature/concentration field coupling relationships [15]. Wang et al. carried out the flow field and temperature field simulation, calculation and analysis in terms of depyrogenation tunnel, a very popular preparation drying-sterilization equipment in pharmaceutical processes [16].

3. RESEARCH METHODOLOGY

3.1 Experimental settings

The experiment focused on a small rubber-roll husker, aiming to precisely analyse the temperature and airflow distribution within its husking chamber. The husking chamber's front face was defined as the XOY plane, with the lateral direction designated as the Z-axis. Three cross-sections on the XOY plane were selected as monitoring targets, centred at the chamber's coordinate origin (0, 0, 0). Section 1 was positioned at the plane 50 mm along the Z direction, section 2 coincided with the coordinate origin plane, and section 3 was located at the plane 50 mm along the Z direction.

Based on experimental results of temperature and airflow velocity in the husking chamber, this study evaluates the distribution patterns of the temperature field and flow field within the chamber. These findings provide boundary conditions for numerical simulations of the temperature and flow fields. By comparing scalar experimental values (temperature and airflow velocity) with corresponding numerical simulation results, the accuracy and rationality of the finite element simulation model are validated.

(1) Temperature detection

The temperature distribution within the husking chamber was tested using a UTi260B thermal imaging camera, with measurements focused on the temperature of the husking rubber roller zone and the suction inlet, as illustrated in Fig. 1. Tables I, II, and III list the temperature values at measurement points on sections 1, 2, and 3, respectively.

Figure 1: Schematic diagram of temperature detection point in the hulling chamber.

Table I: The temperature values of each measuring point on section 1 of the XOY plane (°C).

Frequency	Measuring point					
	1	2	3	4	5	6
1	21.0	44.8	43.0	50.0	44.0	44.0
2	19.0	49.0	46.0	56.0	49.0	50.0
3	21.1	45.8	43.5	55.1	45.2	43.6
4	22.0	46.4	42.0	54.0	46.0	44.0
5	20.6	46.0	45.0	55.0	47.0	48.0

Table II: The temperature values of each measuring point on section 2 of the XOY plane (°C).

Frequency	Measuring point					
	1	2	3	4	5	6
1	30.0	49.6	48.0	58.0	52.0	51.0
2	29.0	52	47.6	57.4	51.4	50.6
3	28.3	49.8	46.1	56.2	50.0	49.0
4	26.0	50.0	44.0	55.5	48.0	48.5
5	27.6	48.0	45.0	54.8	48.6	47.8

Table III: The temperature values of each measuring point on section 3 of the XOY plane (°C).

Frequency	Measuring point					
	1	2	3	4	5	6
1	29.0	44.0	45.7	55.0	51.0	47.0
2	28.4	43.5	44.6	55.7	50.8	46.6
3	27.0	42.3	43.5	54.9	49.4	45.6
4	26.0	41.0	43.0	54.0	48.6	45.0
5	25.8	41.5	42.0	53.8	48.5	44.7

A comparative analysis of Tables I to III reveals that all temperature values measured on section 2 (the central plane of the husking chamber) are higher than those on sections 1 and 3. This phenomenon occurs because section 2 corresponds to the chamber's central zone, where rice grains predominantly accumulate during the operation of the husking rubber rollers, resulting in elevated temperatures in this region due to concentrated friction and compression forces.

(2)Velocity vector detection

The DT-8880 thermal anemometer was used to measure airflow velocities at the primary suction inlet and outlet of the husking chamber. To comprehensively establish the velocity field within the husking chamber, five key monitoring points in the chamber were selected as experimental measurement points, as shown in Fig. 2. The experiment measured airflow velocities at these five points across the three cross-sections.

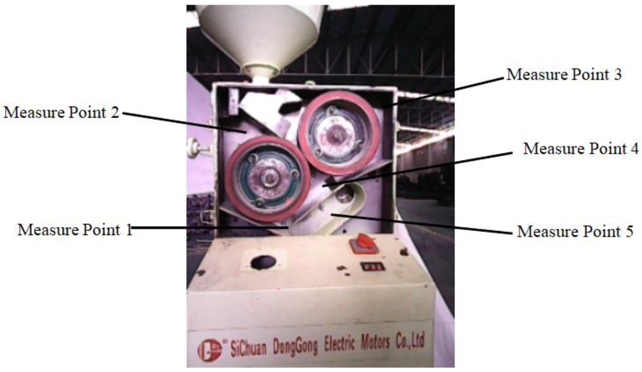

Figure 2: Schematic diagram of velocity vector detection points in the hulling chamber.

Table IV: The velocity values of each measuring point on section 1 of the XOY plane (m/s).

Frequency	Measuring point				
	1	2	3	4	5
1	4.69	1.51	3.45	1.07	15.68
2	4.68	1.20	3.22	0.96	15.80
3	4.98	1.38	3.02	1.11	15.79
4	4.50	1.46	2.91	1.26	15.31
5	4.46	1.38	3.07	1.42	15.27

Table V: The velocity values of each measuring point on section 2 of the XOY plane (m/s).

Frequency	Measuring point				
	1	2	3	4	5
1	4.58	3.24	6.44	1.00	16.07
2	4.06	3.68	6.50	1.40	17.37
3	4.31	3.44	6.89	1.20	16.38
4	4.30	3.55	6.95	1.15	15.90
5	4.69	3.60	7.20	1.34	16.50

Table VI: The velocity values of each measuring point on section 7 of the XOY plane (m/s).

Frequency	Measuring point				
	1	2	3	4	5
1	4.12	2.15	5.60	1.48	18.00
2	3.95	2.04	5.54	1.67	16.59
3	4.08	2.04	5.35	1.53	17.37
4	3.90	1.96	5.16	1.48	17.04
5	4.35	1.97	2.09	1.50	16.83

Comparative analysis of Tables IV to VI indicates that the velocity trends across the five monitoring points on the three selected sections are generally consistent. The velocity magnitudes at all monitoring points within the husking chamber are relatively low, with point 4 exhibiting the lowest velocity and point 5 the highest. When airflow enters the suction channel of the husking chamber under the action of the suction centrifugal fan, it undergoes intense collisions with the channel walls. The airflow gradually accelerates along the channel walls and may form vortices. The air within the channel carries numerous rice husks, which can become trapped and accumulate in the channel. When the fresh rice mill stops operating, these residual husks flow into the brown rice hopper through the channel, potentially increasing the impurity rate (e.g., residual husks) in the processed brown rice

3.2 The numerical simulation

The research focuses on a rubber-roll husker, where husk separation is achieved through the differential rotational speeds of two counter-rotating rubber rollers. The friction and compressive forces generated between the roller surfaces separate rice husks from brown rice. The counter-rotating motion of the rollers induces high-speed rotational airflow near their surfaces, creating localized vortices within the husking chamber. After analysing the advantages and limitations of various turbulence models in Table VII, the realizable *k*-*ε* model was selected for simulating the temperature and flow fields in the husking chamber [17].

Table VII: Comparison of advantages and disadvantages of various turbulence models.

Model name	Advantage	Shortcoming
Spalart-Allmaras	It is suitable for the case of low Relo number and complex boundary	The solution equation is single and cannot be used in uniform decay and isotropic turbulence
Standard *k*-*ε* model	Suitable for moderate calculation, high versatility, high accuracy	The solution of complex working conditions is unstable, the pressure gradient has vorticity, and the quality of numerical simulation results is low
Realizable *k*-*ε* model	It has the advantages of high reliability, high calculation accuracy and stable solution of rotating basin	There are limitations to the hypothesis of isotropy of cyclic viscosity
Reynolds stress model	Suitable for complex flows with high accuracy	The calculation time is long and the computer configuration requirements are high

The numerical simulation domain for the rubber-roll husker focuses on the husking chamber. To enhance simulation efficiency, geometric modelling omitted the influence of auxiliary components such as screws, bolts, nuts, and latches. Key functional parts – including the husking rubber rollers, inclined chute, feeding roller, and guide plate – were simplified appropriately. The simplified 3D model, shown in Fig. 3, retains the core components: husking rubber rollers, guide plate, inclined chute, feeding roller, and the husking chamber enclosure. In Fig. 3, the transparent structure represents the outer shell contour of the husking chamber.

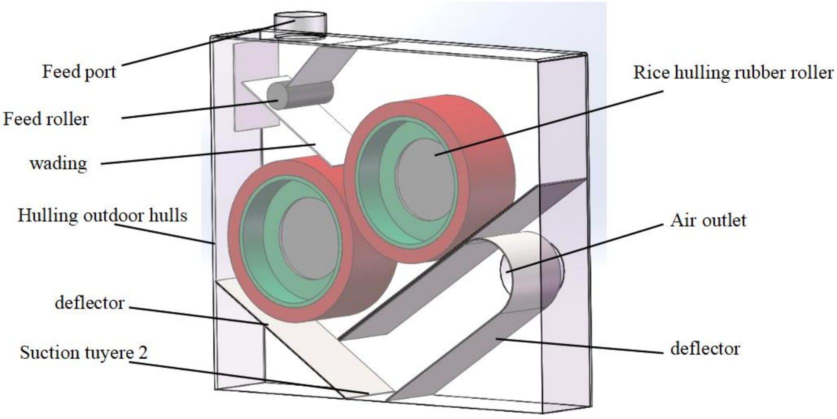

Figure 3: Simplified model of hulling chamber.

This study employed ANSYS ICEM-CFD to mesh the fluid domain of the husking chamber. To enhance overall mesh quality and computational accuracy in numerical simulations, the fluid domain model was partitioned into sub-regions for meshing, including the feed inlet, suction inlet, husking rubber rollers, and guide plate. A structured hexahedral mesh was adopted, with a grid size of 5 mm for the rubber rollers and guide plate, and 4 mm for the feed inlet and suction inlet. The final mesh of the entire fluid domain within the husking chamber comprised 1,553,629 nodes and 1,107,823 elements.

Mesh quality was evaluated using the ANSYS Workbench Meshing module. Key mesh quality metrics (e.g., skewness, aspect ratio) were analysed via the Mesh Metric tool under the Quality dropdown menu. As summarized in Table VIII, all mesh quality parameters for the fluid domain fell within the acceptable thresholds defined by finite element analysis standards. This confirms that the generated mesh satisfies quality requirements and is suitable for subsequent numerical simulations.

Table VIII: Grid quality parameters of flow field in hulling chamber.

Mesh quality parameter	Parameter value
Element quality	0.845
Aspect ratio	1.81
Jacobian ratio	1.02
Skewness	0.15
Orthogonal quality	0.85

Experimental analysis of the temperature and flow fields in the rubber-roll husking chamber revealed that during rice processing, elevated temperatures within the chamber are concentrated near the husking rubber rollers. Structural analysis confirms that the primary heat source stems from frictional heat generation during the interaction of the two counter-rotating rollers. In ANSYS Meshing, boundary definitions were implemented as follows: The Named Selection tool was employed to designate the end faces of the two husking rollers as heat 1 and heat 2, representing heat sources. Airflow direction analysis guided the assignment of the suction inlet and air outlet boundaries: the suction port face was labelled inlet, and the outlet face outlet, as illustrated in Fig. 4. Detailed boundary condition parameters, including velocity, pressure, and thermal inputs, are listed in Table IX for simulation configuration.

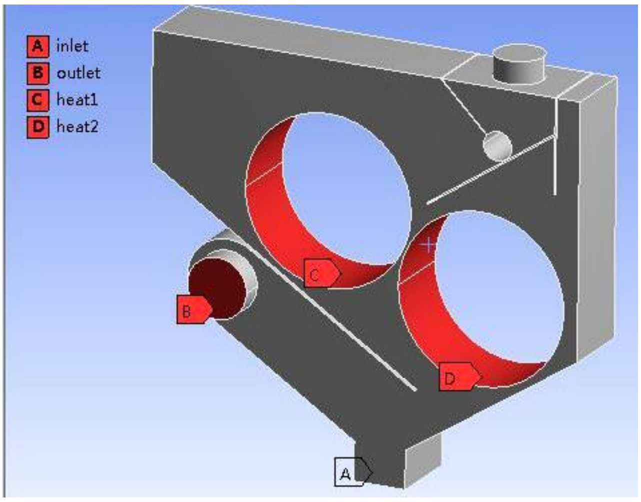

Figure 4: Boundary setting.

Table IX: Boundary condition parameters.

Boundary setting	Boundary condition type	Size	Hydraulic diameter	Temperature	Centre point position
Inlet	Velocity-inlet	14 m/s	0.08296	7	/
Outlet	Pressure-outlet	/	0.08	/	/
Wall 1	Rotational wall	65 rad/s	/	60	(-0.067, 0.414, 0.052)
Wall 2	Rotational wall	99 rad/s	/	55	(0.141, -0.052, 0.052)

4. RESULTS AND DISCUSSION

4.1 Analysis of numerical simulation results

The numerical simulation results primarily analyse the temperature field and flow field distributions within the husking chamber. The study focuses on temperature contours and velocity vector plots to evaluate the magnitude and spatial variations of temperature and airflow inside the rubber-roll husker. By comparing discrepancies between numerical predictions and experimental measurements, the validity of the selected turbulence model and boundary condition configurations is verified. This analysis provides critical insights for refining optimization strategies and boundary condition settings in subsequent husking chamber design improvements.

To investigate the influence of temperature within the husking chamber on the broken rice rate during husking, CFD-POST post-processing software was utilized to analyse the temperature field distribution after completing the Fluent numerical simulations. Fig. 5 a illustrates the overall temperature contour map within the husking chamber, while Figs. 5 b, c, and d display the temperature distribution contours for sections 1, 2, and 3, respectively.

A comparative analysis of the temperature contour maps from sections 1, 2, and 3 reveals broadly consistent temperature distribution patterns across all three cross-sections of the husking chamber. Focusing on section 2 (the central plane) as the primary analytical target, the temperature contour map clearly illustrates the thermal profile within the chamber. Elevated temperatures are concentrated near the husking rubber rollers, with the highest temperatures observed at the roller edges (approximately 60 °C). Moderately high temperatures occur in the region between the guide plate and the rollers, while the lowest temperatures are found along the suction inlet near the guide plate, demonstrating a gradual thermal gradient from the roller contact zones to the airflow-driven cooling areas.

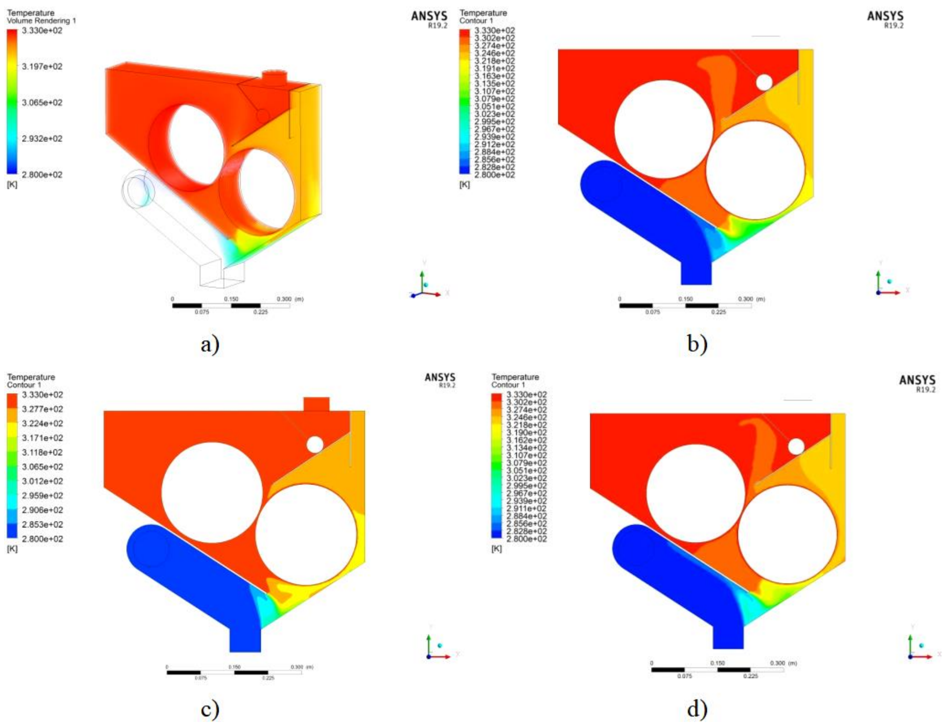

Figure 5: a) Temperature cloud map of rice hulling chamber, b) Temperature cloud map of section 1 of the rice hulling chamber, c) Temperature cloud map of section 2 of the rice hulling chamber, d) Temperature cloud map of section 3 of the rice hulling chamber.

To visually and clearly observe and analyse the internal flow field distribution within the husking chamber, the velocity field was obtained using CFD-POST post-processing software after completing the Fluent numerical simulation. Figs. 6 a, b, and c show the velocity contour maps for sections 1, 2, and 3 of the husking chamber, respectively.

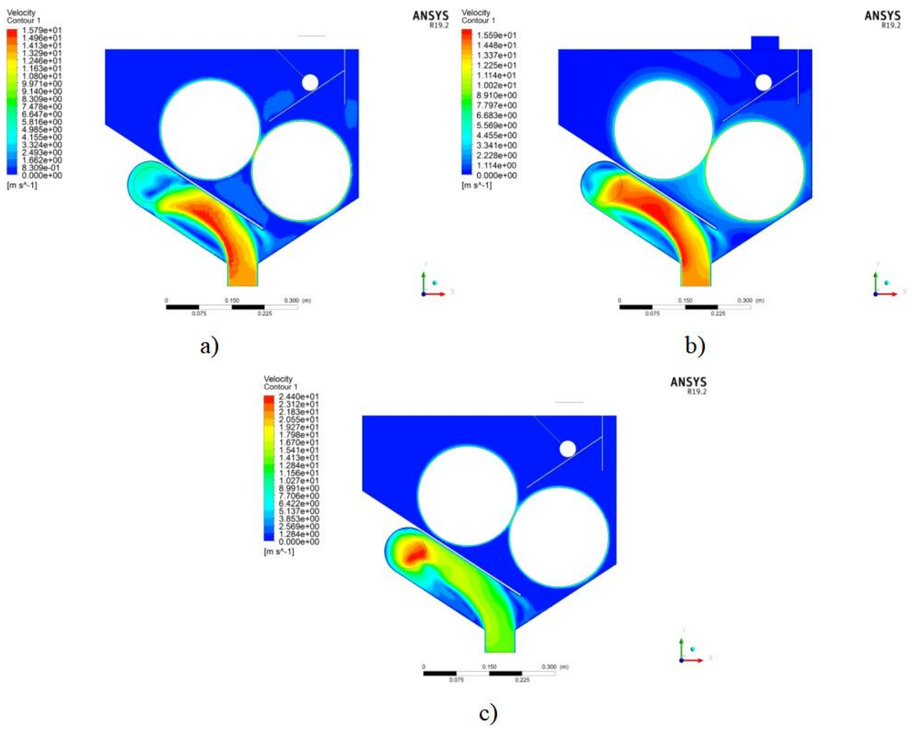

Figure 6: a) Velocity cloud diagram of hulling chamber section 1, b) Velocity distribution in the section 2 of the hulling chamber, c) Velocity distribution in the section 3 of the hulling chamber.

A comparative analysis of the velocity contour maps from sections 1, 2, and 3 reveals that the airflow velocity in section 2 (central plane) of the husking chamber is notably higher than in sections 1 and 3. Focusing on section 2 for detailed analysis, it is evident that as airflow enters the chamber through the suction inlet, its velocity peaks at the inlet location. The velocity further increases in the region spanning from the guide plate to the outlet, reaching a maximum of 15.6 m/s. Overall, the airflow velocity within the husking chamber ranges between 1.2 m/s and 15.6 m/s, with distinct spatial variations driven by the interaction between the suction force, structural components, and rotational motion of the rollers.

To visually and clearly observe and analyse the internal flow field distribution within the husking chamber, the velocity vector field was obtained using CFD-POST post-processing software after completing the Fluent numerical simulation. Figs. 7 a, b, and c illustrate the velocity vector distributions for sections 1, 2, and 3 of the husking chamber, respectively.

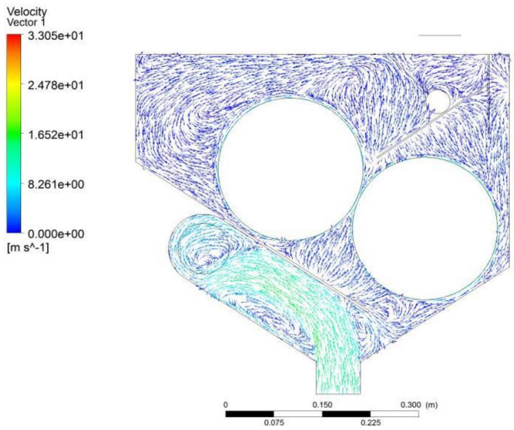

a)

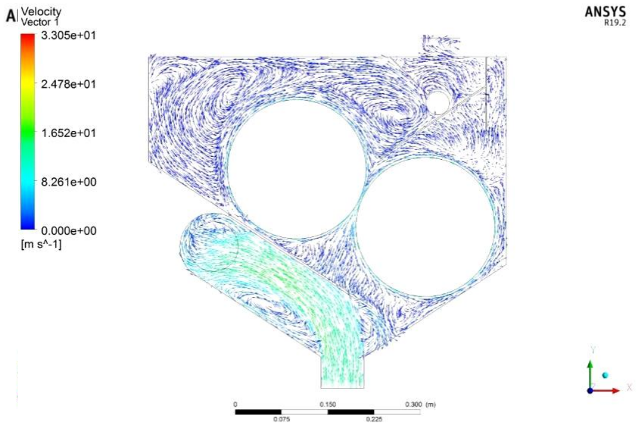

b)

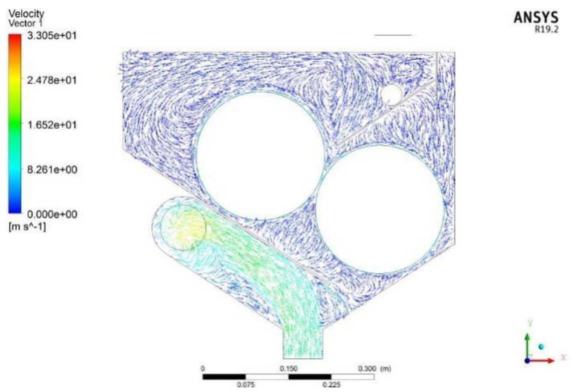

c)

Figure 7: a) Velocity vector diagram of section 1 of the rice hulling chamber, b) Velocity vector diagram of section 2 of the rice hulling chamber, c) Velocity vector diagram of section 3 of the rice hulling chamber.

A comparative analysis of velocity vector diagrams across three cross-sections (1, 2, 3) shows consistent airflow patterns in the husking chamber. Focusing on section 2, higher velocities occur between the suction inlet/outlet near the guide plate and around the husking rubber rollers, with lower speeds elsewhere. Reduced outlet cross-sectional area accelerates airflow, causing wall collisions and backward flow that form vortices in the suction channel. Most airflow originates from the inlet, while minimal near the rollers is extracted by the centrifugal fan. Counter-rotating rollers also drive airflow, generating wall-collision-induced vortices along chamber surfaces.

4.2 Experimental vs. numerical results: a comparative analysis

Fig. 8, which compares experimental measurements with simulated values, demonstrates that the temperature trends across sections 1, 2, and 3 align closely between experimental and numerical results. Notably, simulated temperatures at measurement point 4 (located near the husking rollers) consistently show the highest values among all measurement points, consistent with the operational behaviour of the rubber-roll husker under real-world conditions. The relative errors between experimental and simulated temperature values across all measurement points range from 0.4 % to 13.5 %, with 80 % of the data points exhibiting errors within the 0.4 %–10 % range. This error distribution confirms that the selected turbulence model and boundary condition configurations for the temperature field simulation are rationally formulated and effectively capture the thermal dynamics of the husking chamber.

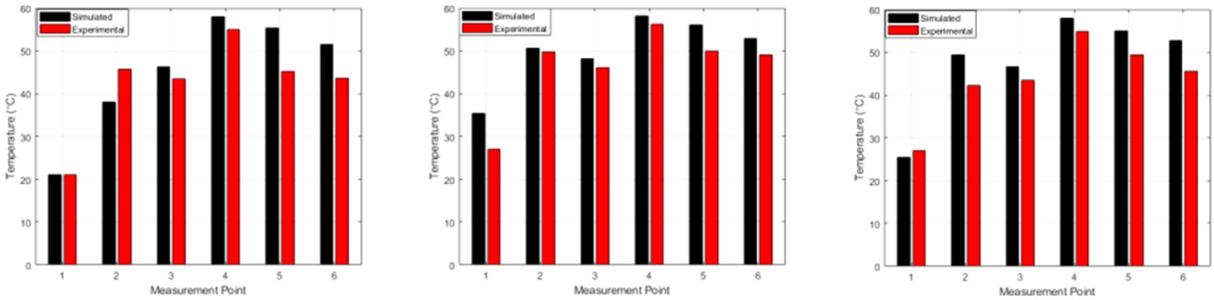

a) Section 1 b) Section 2 c) Section 3

Figure 8: Comparison chart between temperature test detection values and simulated values.

Experimental analysis indicates that potential sources of error may include:

(1) Impact of test conditions: The experiments were conducted during winter, and the influence of indoor temperature variations was not accounted for, which may introduce certain deviations in the experimental results.

(2) Measurement errors: During practical testing, discrepancies in temperature values may arise when capturing thermal images of the husking chamber using an infrared thermal imager due to differences in shooting angles and methodologies.

(3) Geometric modelling simplifications: The geometric model neglected the effects of auxiliary components such as screws, bolts, nuts, and latches. Additionally, functional parts like the husking rollers, inclined chute, guide plate, and feeding roller were simplified, potentially reducing the fidelity of the simulation compared to the actual system.

These factors collectively contribute to the observed discrepancies between experimental and simulated outcomes.

Fig. 9, which compares experimental measurements with simulated velocity scalar values, demonstrates that the velocity trends across sections 1, 2, and 3 align closely between experimental and numerical results. Notably, simulated velocities at measurement point 5 (located in the high-speed airflow region near the outlet) consistently show the highest values among all measurement points, which aligns with the operational characteristics of the rubber-roll husker under real-world conditions. The relative errors between experimental and simulated velocity scalar values across all measurement points are within 15 %. This error range confirms that the turbulence model and boundary condition configurations selected for the velocity field simulation are rationally designed and effectively reflect the airflow dynamics within the husking chamber.

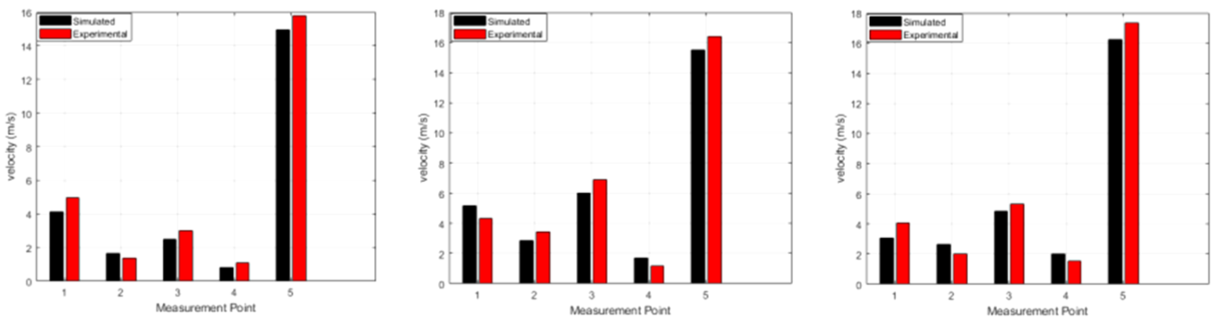

a) Section 1 b) Section 2 c) Section 3

Figure 9: Comparison chart of speed vector test detection values and simulated values.

Experimental analysis indicates that potential sources of error may include:

(1) Process-related issues in the test model: Gaps exist between the hatch door of the experimental husking chamber and the chamber itself. During operation, external air infiltrates through these gaps, altering the internal flow field distribution.

(2) Measurement errors: During testing, the presence of five inspection holes on the chamber walls affects the flow field of the dust removal system, thereby compromising the accuracy of experimental measurements.

(3) Impact of geometric model simplifications: The geometric model for the internal flow field neglected the influence of auxiliary components (screws, bolts, nuts, latches) and simplified functional parts (husking rollers, inclined chute, guide plate, feeding roller). These simplifications may omit subtle effects of the components on the flow dynamics.

(4) Other factors: Unaccounted variables during testing, such as ambient temperature fluctuations, centrifugal fan characteristics, air leakage in the husking chamber, and variations in air density, could also contribute to discrepancies.

These factors collectively explain deviations between experimental and simulated results, highlighting areas for refinement in future experimental and modelling protocols.

5. CONCLUSION

Through comprehensive analysis and experimental investigations of the temperature and flow fields in the hulling chamber of a rubber-roller paddy huller, the following conclusions are drawn:

(1) Experimental measurements of the hulling chamber's temperature and flow fields revealed a maximum temperature of 55.9 °C at the roller engagement point on section 2, with a minimum temperature of 21 °C. Comparative analysis of temperature variations across six monitoring points on three cross-sections showed consistent temperature trend curves. Velocity measurements at five monitoring points across the sections demonstrated uniform flow patterns, with the maximum airflow velocity (17.37 m/s) observed in the chamber's exhaust duct.

(2) Numerical simulations conducted using ANSYS Fluent software delineated the temperature and velocity vector distributions under operational conditions. Results indicated elevated temperatures near the rubber rollers, peaking at ~60 °C along roller edges. Flow field analysis identified recirculation vortices forming at the air intake, exhaust ports, and roller interaction zones.

(3) Comparative validation between experimental and simulated data confirmed the accuracy of the temperature and flow field models. Temperature deviations remained within 13.5 %, while velocity vector errors did not exceed 15 %, demonstrating the reliability of the numerical simulation methodology for coupled thermal-fluid analysis.

REFERENCES

[1] Corrêa, P. C.; da Silva, F. S.; Jaren, C.; Afonso Júnior, P. C.; Arana, I. (2007). Physical and mechanical properties in rice processing, *Journal of Food Engineering*, Vol. 79, No. 1, 137-142, doi:10.1016/j.jfoodeng.2006.01.037

[2] Lu, Y.; Li, X. (2005). Progress in study of protein denaturation and thermodynamic parameters of denaturation, *Progress in Chemistry*, Vol. 17, No. 5, 905-910

[3] Zeng, Y.; Jia, F.; Meng, X.; Han, Y.; Xiao, Y. (2018). The effects of friction characteristic of particle on milling process in a horizontal rice mill, *Advanced Powder Technology*, Vol. 29, No. 5, 1280-1291, doi:10.1016/j.apt.2018.02.021

[4] Wang, L.; Yu, N.; Fan, J.; Zhang, Y.; Pei, H.; Zhang, Y. (2020). Simulation of separation of rice bran and broken rice in top-suction rice mill with annular duct, *Proceedings of the 2020 3rd International Conference on E-Business, Information Management and Computer Science*, 398-402, doi:10.1145/3453187.3453367

[5] Sfeir, A. A. (1976). The velocity and temperature fields of rectangular jets, *International Journal of Heat and Mass Transfer*, Vol. 19, No. 11, 1289-1297, doi:10.1016/0017-9310(76)90081-8

[6] Hao, L.; Wang, L.; Li, H. P.; Liu, P. P. (2024). Simulation inspection technology for surface characteristics of high-quality strips, *International Journal of Simulation Modelling*, Vol. 23, No. 3, 459-470, doi:10.2507/IJSIMM23-3-693

[7] Kevorkijan, L.; Pezdevsek, M.; Bilus, I.; Hren, G. (2023). Cavitation erosion modelling – comparison of different driving pressure approaches, *International Journal of Simulation Modelling*, Vol. 22, No. 2, 233-244, doi:10.2507/IJSIMM22-2-639

[8] Rahimi-Esbo, M.; Rahgoshay, S. M.; Hassani, M. M.; Dadashi Firouzjaei, K. (2020). Novel design and numerical evaluating of a cooling flow field in PEMFC with metallic bipolar plates, *International Journal of Hydrogen Energy*, In press, 12 pages, doi:10.1016/j.ijhydene.2020.07.066

[9] Pastohr, H.; Kornadt, O.; Gürlebeck, K. (2004). Numerical and analytical calculations of the temperature and flow field in the upwind power plant, *International Journal of Energy Research*, Vol. 28, No. 6, 495-510, doi:10.1002/er.978

[10] Li, W.; Zhang, Q.; Wang, C.; Yan, X.; Shen, S.; Xia, G.; Zhu, F.; Zhang, J. (2017). Experimental and numerical analysis of a three-dimensional flow field for PEMFCs, *Applied Energy*, Vol. 195, 278-288, doi:10.1016/j.apenergy.2017.03.008

[11] Zhou, T.; Rempfer, D. (2013). Numerical study of detailed flow field and performance of Savonius wind turbines, *Renewable Energy*, Vol. 51, 373-381, doi:10.1016/j.renene.2012.09.046

[12] Xiang, R. B.; Lee, K. W. (2005). Numerical study of flow field in cyclones of different height, *Chemical Engineering and Processing: Process Intensification*, Vol. 44, No. 8, 877-883, doi:10.1016/j.cep.2004.09.006

[13] Salaheldin, T. M.; Imran, J.; Chaudhry, M. H. (2004). Numerical modeling of three-dimensional flow field around circular piers, *Journal of Hydraulic Engineering*, Vol. 130, No. 2, 91-100, doi:10.1061/(ASCE)0733-9429(2004)130:2(91)

[14] Kumar, V.; Nigam, K. D. P. (2005). Numerical simulation of steady flow fields in coiled flow inverter, *International Journal of Heat and Mass Transfer*, Vol. 48, Nos. 23-24, 4811-4828, doi:10.1016/j.ijheatmasstransfer.2005.05.037

[15] Lim, K.; Lee, C. (2008). A numerical study on the characteristics of flow field, temperature and concentration distribution according to changing the shape of separation plate of kitchen hood system, *Energy and Buildings*, Vol. 40, No. 2, 175-184, doi:10.1016/j.enbuild.2007.02.028

[16] Wang, Y.; Zhu, Q.; Huang, T.; Han, X.; Lin, M. (2024). Modelling and simulation of nonlinear dynamic flow field and temperature field of depyrogenation tunnel, *Facta Universitatis, Series: Mechanical Engineering*, Vol. 22, No. 1, 45-62, doi:10.22190/FUME221221011W

[17] Li, W.; Su, M. (2006). Common turbulence models and their applications in FLUENT software, *Pump Technology*, Vol. 2006, No. 4, 39-40